JPE

An Active Damping Scheme Based on a Second Order Resonant Integrator for *LCL*-Type Grid-Connected Converters

Chen Chen*, Jian Xiong†, and Kai Zhang*

†*State Key Laboratory of Advanced Electromagnetic Engineering and Technology, School of Electrical and Electronic Engineering, Huazhong University of Science and Technology, Wuhan, China

Abstract

This paper proposes a novel active damping scheme to suppress *LCL*-filter resonance with only grid-current feedback control in grid-connected voltage-source converters. The idea comes from the concept of the model reference adaptive control (MRAC). A detailed theoretical derivation is given, and the effectiveness of this method is explained based on its physical nature. According to the control structure of this method, the active damping compensator, which is essentially a second order resonant integrator (SORI) filter, provides an effective solution to damp *LCL* resonance and to eliminate the need for additional sensors. Compared with extra feedback methods, the cost and complexity are reduced. A straightforward tuning procedure for the active damping method has been presented. A stability analysis is illustrated in the discrete domain while considering a one-step delay. Finally, experimental results are presented to validate the analysis and to demonstrate the good performance of the proposed method.

Key Words: *LCL* filter, model reference adaptive control, resonance damping, grid-connected converter

I. INTRODUCTION

Nowadays, distributed power generation systems (DPGSs) based on renewable energy, such as solar energy and wind energy, are drawing more and more attention due to their environmental friendly features. A grid-connected converter is an important interface between a renewable energy source and the grid. *LCL* line filters are increasingly being used, since they can provide a significantly improved attenuation of the pulse width modulation (PWM) switching harmonics with a reduced overall size and weight when compared with more conventional *L*-filters [1]. However, an *LCL* filter can cause stability problems due to the undesirable resonance caused by the zero impedance at certain frequencies. In order to stabilize such systems, different passive and active damping methods have been proposed [2]-[8].

By adding resistors to the filter capacitors or inductors, passive damping methods are very simple and highly reliable. However, the additional resistors result in power loss and weaken the attenuation ability of *LCL* filters [2], [9]. This shortcoming can be overcome by employing active damping techniques. There are two main active damping techniques. One is to introduce a digital filter with a current controller. The other one is realized by feeding back the filter state variables. The former does not require additional sensors. However, it is sensitive to parameter variations and uncertainties. By introducing extra feedback to provide a damping effect, the active damping methods are also effective. The extra feedback state(s) can be either a single variable, e.g., filter capacitor current or voltage [5], or multiple state variables [6]. These additional feedback-based active damping methods are simple, effective and flexible. However, since more than one feedback state variable is required, the cost increases. Meanwhile, the co-design of the current controller and active damper becomes complex.

Simple but effective single current loop control strategies, which use the same sensors as *L* filters, are promising [10]-[12]. These control methods have become popular in industrial applications. Making the overall system stable is the basic requirement of a control strategy. In the case of a single current loop control strategy, both the inverter-side current and the grid-side current can be used for feedback. Considering the digital control delay, the stability is analyzed for different ratios between the sampling and resonance frequencies of *LCL* filters [11]. The conclusion is that the system cannot be stable without additional active resonance damping when the inverter-side current is used for feedback.

Meanwhile, for grid-side current control, the overall system can be stable as long as the resonance frequency f_r is less than half and more than a quarter of the sampling frequency f_s. Yin *et al*. [12] explores the system stability region through Nyquist diagrams. Several common controllers were applied in a grid-side current loop control strategy. According to [12], when a proportional (P) controller is applied, the conclusion for system stability is that the resonance frequency should be in the region of ($1/6f_s$, $1/2f_s$). In short, with the single current feedback, the cost is low, and the stability is guaranteed if the current sensors or filter parameters are specific. However, due to a high resonance peak, it is still hard to obtain a high bandwidth. Only under the premise of suppressing the resonance peak can a high bandwidth and good robustness be realized simultaneously.

In [13], a model reference adaptive state feedback control is employed to guarantee system stability with wide-range variation of the grid impedance. With this method, the current controller demonstrates good dynamic performance and stability features for grid-tie converters subjected to large grid impedance variations and grid voltage disturbances. Nevertheless, the design procedure for an adaptive state feedback controller is complicated and it requires more sensors. This paper proposes a novel active damping method to suppress the resonance peak with only grid-current feedback control. The proposed active damping method is an adaptive algorithm based on the MRAC, which has the same measurements as an *L* filter. With the proposed controller, it is possible to select a reference model such that the closed-loop system behaves like this model in the steady state. The objective of the MRAC is to ensure the output of a controlled system to track the output of a given reference model system. In addition, it should ensure closed-loop stability. The reference model has a good resonance damping characteristic.

This paper is organized as follows. Section II derives a model of an *LCL*-type grid-connected converter with a single grid-side current control. Three different ratios of the resonance frequency to the sampling frequency have been investigated. Section III presents the derivation of the model reference adaptive system. It also shows the similarities in performance between the reference model and the adaptive model. The essential feature of the proposed active damping method is stated. This adaptive output feedback control is used to introduce a SORI filter. The SORI filter is an alteration of a second-order generalized integrator (SOGI) layout which has been used for building the quadrature signal generator (QSG) in [14]-[16]. The quadrature signals produced by a SOGI-QSG can be used in many applications. For instance, a SOGI-QSG was configured as a SOGI-phased-locked loop (SOGI-PLL) in [14]-[16] for grid synchronization. The SOGI-frequency-locked loop (SOGI-FLL) in [17] was used for frequency estimation. The double SOGI-QSGs (DSOGI-QSG) in [18] was used for the extraction of symmetrical components, and the multiple SOGI-QSG (MSOGI-QSG) in [19] was used for harmonic extraction. In addition, the SOGI algorithm is easy to implement and it can filter input signals without a delay due to its natural resonance at the fundamental frequency [20]-[22]. In this paper, the proposed SORI filter can effectively suppress the resonance peak around the resonance frequency. A discrete-time transfer function is derived including a MRAC system. In Section IV, a straightforward design procedure is presented for the proposed active damping method. Furthermore, a design example is given. In Section V, experimental results are presented to validate the theoretical analysis and the effectiveness of the proposed active damping method. Finally, Section VI concludes this paper.

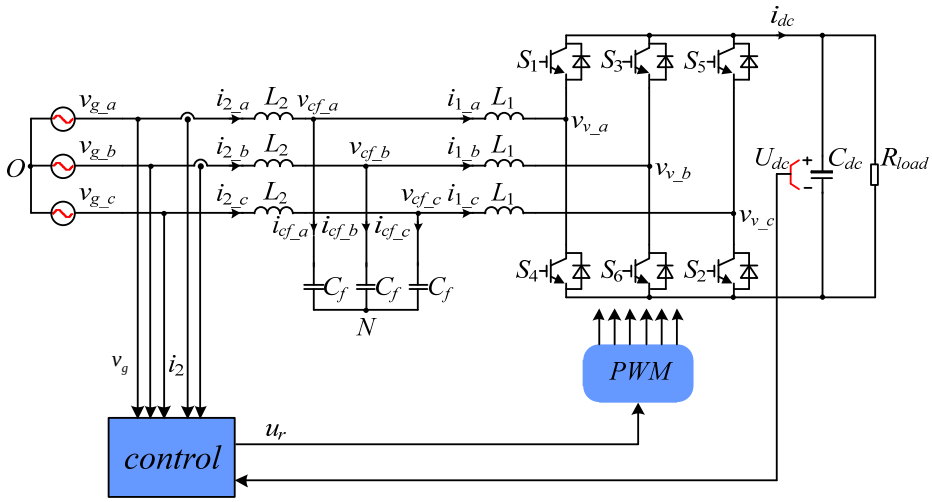

Fig. 1. Schematic diagram of a three-phase *LCL*-type grid connected converter.

II. Modeling and Stability Analysis of the Single Grid Current Control *LCL*-type Grid-connected Converter

A. Modeling of the Single Grid Current Control LCL-type Grid-connected Converter

The system to be analyzed is shown in Fig. 1. A three-phase voltage source converter is connected to the grid through an *LCL* filter. The power switches *S*1-*S*6 and their anti-parallel diodes form the converter. The *LCL* filter consists of converter-side inductors L_1, filter capacitors C_f, and grid-side inductors L_2. The injected grid current i_2 is controlled so that it is in phase with the grid voltage v_g.

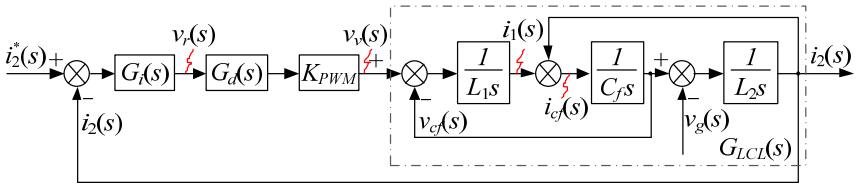

Fig. 2. Per-phase control block diagram of a single grid current feedback control loop.

Generally, the phase angle of v_g is obtained through a phase-locked loop (PLL) [16], [23]. The grid voltage is also been assumed to be balanced, which then allows per-phase diagrams to be used for analysis in Fig. 2. Fig. 2 shows a single grid current feedback control block diagram in the continuous domain, in which the equivalent series resistance of the filtering elements is neglected.

The current amplitude reference i^*_2 is generated by the dc link voltage loop. The current error signal is sent to the current regulator G_i in the stationary $\alpha\beta$ frame. v_r is the output signals of the injected grid current regulators, v_v is the three-phase midpoint voltages of the three converter legs that are referred to point N, v_{cf} is the three-phase ac filter voltages that are referred to point N, i_1 is the three-phase converter-side inductor currents, and i_{cf} is the three-phase ac filter currents. K_{PWM} is the gain of the PWM converter.

A PR regulator is employed considering the overall system dynamics. In the s-domain, a PR regulator is expressed as:

$$G_i(s) = k_p + \frac{2k_r\omega_i s}{s^2 + 2\omega_i s + \omega_o^2} \tag{1}$$

where k_p is the proportional coefficient, k_r is the resonant coefficient, $\omega_o = 2\pi f_o$ is the fundamental angular frequency, f_o is the fundamental frequency, and ω_i is the resonant cutoff frequency. To deal with a typical $\pm$1% variation in the grid fundamental frequency [24], $\omega_i = 1\% \cdot 2\pi f_o = \pi$ rad/s is set.

$G_d(s)$ is a transfer function combing the computation delay, the PWM delay, and the sampler [25]. It is expressed as:

$$G_d(s) = e^{-sT_s} \cdot \frac{1 - e^{-sT_s}}{s} \cdot \frac{1}{T_s} \approx e^{-1.5sT_s} \tag{2}$$

where T_s is the system sampling period.

B. Stability Analysis under Various Resonance Frequencies

According to Fig. 2, the loop gain $T_c(s)$ can be derived as:

$$T_c(s) = G_i(s)G_d(s)K_{PWM}G_{LCL}(s) = \frac{G_i(s)K_{PWM}e^{-1.5sT_s}}{L_1L_2C_f s(s^2 + \omega_r^2)} \tag{3}$$

where ω_r is the resonance angular frequency of the *LCL* filter, which is expressed as:

$$\omega_r = \sqrt{\frac{L_1 + L_2}{L_1L_2C_f}} \tag{4}$$

and the resonance frequency is $f_r = \omega_r/2\pi$.

Due to the existence of a one-step delay, the stability of a single grid current loop system is influenced by the resonance frequency variation. One-sixth of the sampling frequency is a critical frequency [26]. Table I shows the parameters of the converter prototype system for three different cases. Using these parameters and equation (3), Bode diagrams of the loop gain $T_c(s)$ with $G_i(s)$=1 for different values of f_r are shown in Fig. 3. As can be seen, with a variation of f_r, the stability of the loop system varies. For case A, the resonance frequency f_r is higher than the critical frequency $f_s/6$. The phase characteristic crosses -180° outside a region whose amplitude is positive. According to the Nyquist stability criterion, the system is stable. For cases B and C, the system is unstable, because the phase characteristic crosses -180° inside a region whose amplitude is above 0 dB. Then active damping is mandatory to improve the system amplitude characteristic or phase characteristic. For a high resonant frequency region, although active damping is not required, it is hard to obtain a high bandwidth and better robustness. This is especially true for wide-range variations of the *LCL* parameters.

TABLE I. PARAMETERS OF THE PROTOTYPE.

Nominal System Parameters		
L_1=1.25mH	L_2=0.625mH	
Grid line-to-line rms voltage V_{gab} =80V	DC bus voltage U_{dc} =230V	Power rating P_o =1.5kW
Fundamental frequency f_o =50Hz	Switching frequency f_{sw} =5kHz	Sampling frequency f_s =10kHz
AC filter Capacitances and Resonance Frequencies		
Case A	C_f =12μH	f_r =2.25kHz	f_r/f_s =0.225
Case B	C_f =22μH	f_r =1.67kHz	f_r/f_s =0.167
Case C	C_f =50μH	f_r =1.1kHz	f_r/f_s =0.11

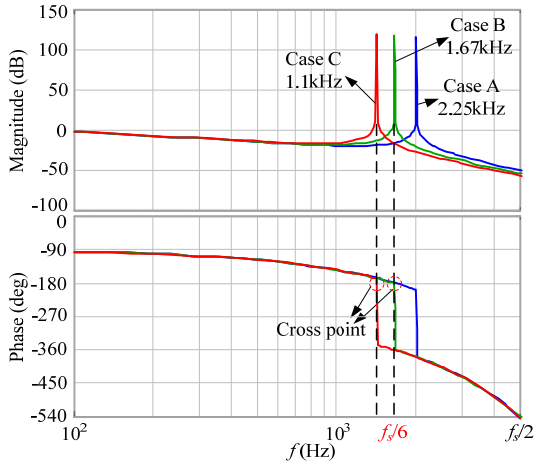

Fig. 3. Bode diagrams of the loop gain $T_c(s)$ with $G_i(s)$=1 for three different cases.

III. PROPOSED ACTIVE DAMPING SCHEME BASED ON A SORI FILTER

A. Derivation of the Proposed Active Damping Scheme

As previously reported, when $f_r \le f_s/6$, a single grid-current control system cannot be stable while considering a one-step

delay. Then an active damping method should be implemented to eliminate the resonance peak. This effectively changes the unstable characteristic around the resonance frequency f_r. This paper proposed a novel active damping

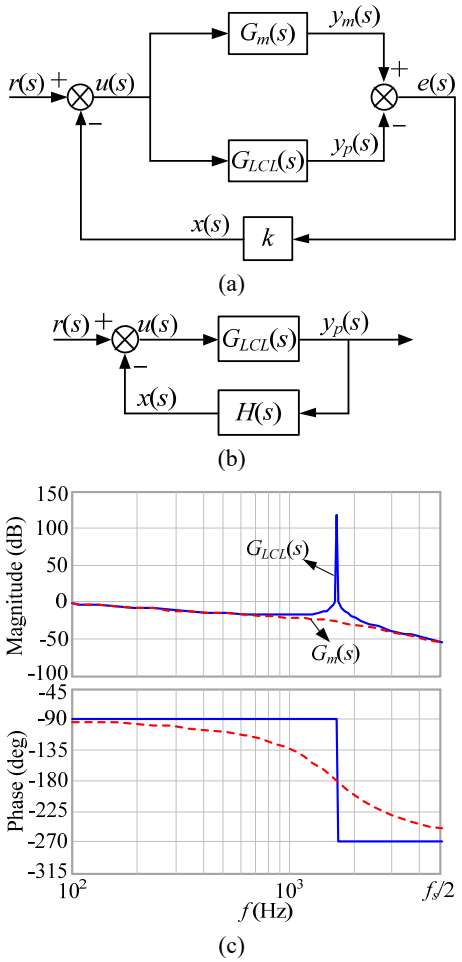

Fig. 4. (a) Model reference output feedback adaptive control structure. (b) Equivalent mathematic model of a MRAC system. (c) Bode diagrams of the adaptive model $G_{LCL}(s)$ and the reference model $G_m(s)$.

method, which introduces a reference model that behaves like an *LCL* model. In addition, it has no resonance peak so that the system can obtain better damping characteristic with single grid current control.

Fig. 4(a) shows the control structure of the model reference adaptive control. $G_{LCL}(s)$ represents the passive "plant" which is called an adaptive model. $G_m(s)$ is the reference model. k is the adaptive law. $e(s)$ is the error component between the adaptive model and reference model output responses, i.e., $e(s)=y_m(s)-y_p(s)$. The control target is to provide the same attenuation and dynamic characteristics as the grid-connected converter. The reference model is chosen as:

$$G_m(s)=\frac{y_m(s)}{u(s)}=\frac{1}{L_1L_2C_fs(s^2+\xi\omega_n s+\omega_n^2)} \tag{5}$$

where ξ is the damping factor, and ω_n is the natural frequency which is equal to the resonance angular frequency ω_r.

Fig. 4(b) is an equivalent mathematic model of a MRAC system. At the resonance frequency f_r, the input signal $r(s)$ has a 180 degree reversal. The reversed signal $y_p(s)$ returns to the input after it is multiplied by an appropriate gain. This feedback system is constituted of the effective active damping. The physical significance of introducing the reference model is that the signal $x(s)$ can play a role in suppressing the resonance peak at around the resonance frequency as observed in Fig. 4(b).

The feedback loop transfer function $H(s)$ is derived as:

$$\begin{aligned}H(s)&=\frac{x(s)}{y_p(s)}=\frac{k[y_m(s)-y_p(s)]}{y_p(s)}=\frac{ku(s)[G_m(s)-G_{LCL}(s)]}{u(s)G_{LCL}(s)}\\&=\frac{k}{G_{LCL}(s)}\left[\frac{1}{L_1L_2C_fs(s^2+\xi\omega_n s+\omega_n^2)}-\frac{1}{L_1L_2C_fs(s^2+\omega_r^2)}\right]\\&=\frac{k}{G_{LCL}(s)}\cdot\frac{-\xi\omega_n s+\omega_r^2-\omega_n^2}{L_1L_2C_fs(s^2+\omega_r^2)(s^2+\xi\omega_n s+\omega_n^2)}\\&=\frac{-k\xi\omega_n s}{s^2+\xi\omega_n s+\omega_n^2}\end{aligned} \tag{6}$$

Obviously, $-H(s)$ is a second order resonant integrator (SORI) filter. In order to compare the differences between the two models, a Bode diagram is shown in Fig. 4(c). In Fig. 4(c), the predefined reference model $G_m(s)$ has no resonance peak up to the Nyquist frequency. It has similar characteristics in low frequency and high frequency regions except near the resonance frequency. Apparently, the phase characteristic varies smoothly which has no risk of instability.

B. SORI Filter

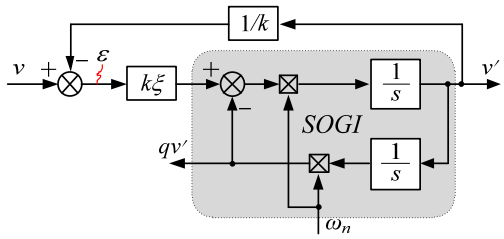

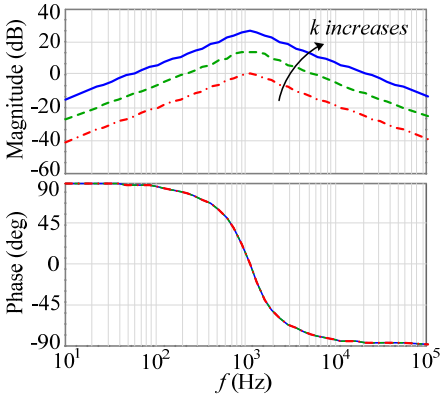

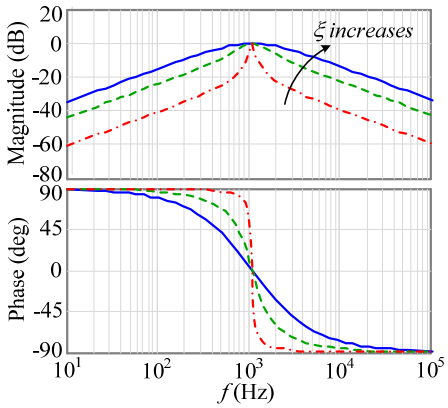

(c)

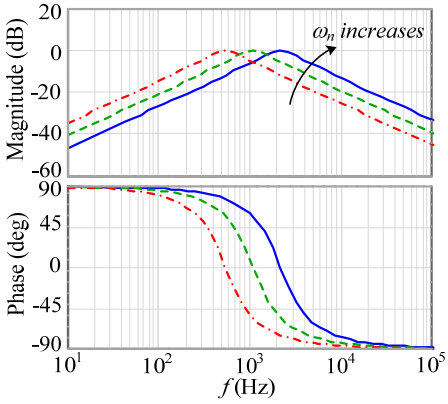

(d)

Fig. 5. SORI filter: (a) Block diagram of the proposed SORI structure (-$H(s)$). (b) Bode diagram of SORI filters when the gain factor k varies. (c) Bode diagram of SORI filters when the damping factor ξ varies. (d) Bode diagram of SORI filters when ω_n varies.

The SORI filter shown in Fig. 5(a), is an alteration of the SOGI layout which has been widely used for implementing grid synchronization. It is based on a frequency-adjustable resonant, which can be implemented by two cascaded integrators working in a closed loop. In addition, it has the advantages of quick and accurate signal-tracking capabilities with good rejection of input signal noise. *v'* and *qv'* represent in-phase and quadrature output signals with a phase shift of 90° with respect to each other. The characteristics of the transfer function -$H(s)$ are different from the classical SOGI, whose Bode plots are shown in Fig. 5(b), 5(c) and 5(d). This depends on three different variables. In Fig. 5(b), when the gain factor increases, the SORI filter amplitude increases. However, the phase characteristic is not affected by the gain factor. Fig. 5(c) shows the variation tendency of the Bode plots when the damping factor varies. Therefore, a small damping factor can make the phase characteristic abruptly change around the resonance frequency f_r. Generally, this is an undesirable case which should be avoided in the design procedure. In Fig. 5(d), the variation of the natural frequency ω_n can only affect the central frequency at which $-H(j\omega)$ peaks at unity gain with a zero phase shift.

Therefore, the design of the SORI filter should consider the three different variables to make the overall system stable and to achieve better dynamic performance.

C. Discrete z-domain Model

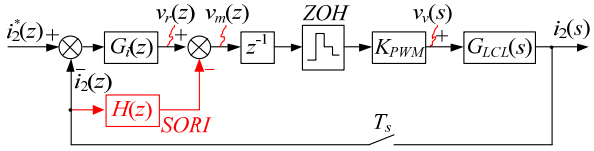

Fig. 6. Control block diagram of the proposed AD scheme in the z-domain.

Fig. 6 illustrates a control block diagram of the proposed AD scheme in the discrete-time domain. v_m represents the modulating signals. A zero-order hold (ZOH) has also been included for modeling the digital pulse width modulation and its accompanied delay. This is inevitable when the continuous system is discretized. Complementing the ZOH block is a z^{-1} delay block included for representing the computational delay. $G_{LCL}(s)$ can be discretized as (7).

$$G_{LCL}(z)=Z_{ZOH}[G_{LCL}(s)]=Z[\frac{1-e^{-sT_s}}{s}\cdot\frac{1}{L_1L_2C_f s(s^2+\omega_r^2)}]$$
$$=\frac{T_s}{(L_1+L_2)(z-1)}-\frac{(z-1)\sin\omega_r T_s}{\omega_r(L_1+L_2)(z^2-2z\cos\omega_r T_s+1)} \quad (7)$$

The PR controller $G_i(s)$ and active damper $H(s)$ can be discretized by applying a bilinear transformation (Tustin method) [29]-[31]. The expressions obtained are as follows:

$$G_i(z)=k_p+\frac{2k_r\omega_i T_s(z-1)}{z^2+z(\omega_o^2T_s^2+2\omega_i T_s-2)-2\omega_i T_s+1} \quad (8)$$

$$H(z)=\frac{-2k\xi\omega_n T_s(z^2-1)}{Az^2+Bz+C} \quad (9)$$

where $A=\omega_n^2T_s^2+2\xi\omega_nT_s+4$, $B=2\omega_n^2T_s^2-8$, and $C=\omega_n^2T_s^2-2\xi\omega_nT_s+4$.

From (7)-(9), the open-loop $T_{col}(z)$ and closed-loop $T_{ccl}(z)$ transfer functions for the grid current control method can be derived as:

$$T_{col}(z)=\frac{G_i(z)z^{-1}K_{PWM}G_{LCL}(z)}{1-z^{-1}K_{PWM}G_{LCL}(z)H(z)} \quad (10)$$

$$T_{ccl}(z)=\frac{G_i(z)z^{-1}K_{PWM}G_{LCL}(z)}{1+[G_i(z)-H(z)]z^{-1}K_{PWM}G_{LCL}(z)} \quad (11)$$

IV. Systematic Design of the Grid Current Control Loop

A. Tuning of the SORI Filter Parameters

The grid current control loop system comprises an inner active damping loop and an outer current regulator loop. Firstly, the active damping loop should ensure stability. The open-loop transfer function of this active damping loop in the continuous domain is given as:

$$T_{ol\_ad}(s)=G_d(s)K_{PWM}G_{LCL}(s)H(s) \quad (12)$$

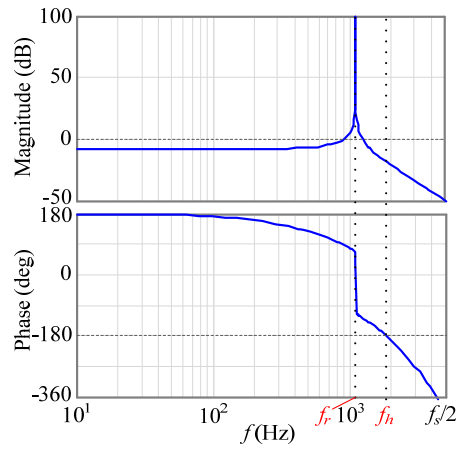

(a)

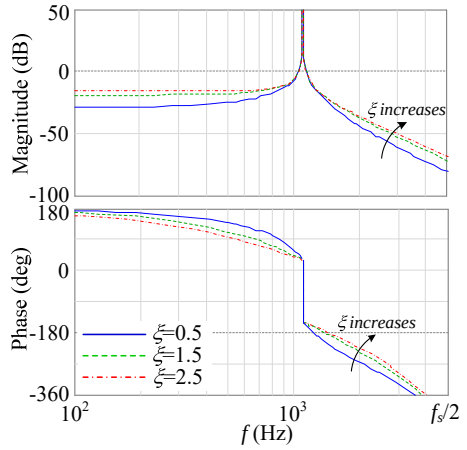

(b)

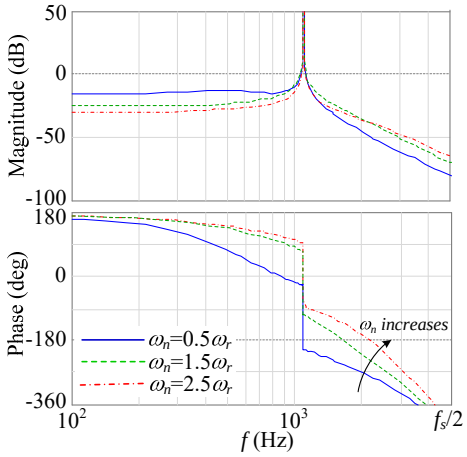

(c)

Fig. 7. Bode diagrams of the inner active damping loop $T_{ol\_ad}(s)$: (a) Stability criteria of the inner active damping loop. (b) Variation of the damping factor ξ. (c) Variation of the natural frequency ω_n.

The design of the active damping loop is mainly the selection of the SORI filter parameters. Because the SORI filter has three different parameters, some design criterion should be provided. A Bode diagram of the inner active damping loop gain $T_{ol\_ad}(s)$ is shown in Fig. 7(a). In the Appendix, the magnitude and phase of $T_{ol\_ad}(s)$ are derived as (A.1) and (A.2), respectively. As can be seen, the phase sharply changes at the resonance frequency f_r. That is to say, the phase starts from 180° at $f = 0$, and crosses over −180° at the frequency f_h. Here the resonance frequency f_r and cross-over frequency f_h are important frequencies. In order to ensure the stability of the inner active damping loop, the cross-over frequency f_h should be larger than f_r to avoid negative crossing at f_r. Around the resonance frequency, the magnitude of $T_{ol\_ad}(s)$ is larger than 0 dB. In addition, at the cross-over frequency f_h, the magnitude is lower than 0 dB. This means that the magnitude frequency characteristic crosses 0 dB in $[f_r, f_h]$. As explained above, the basic condition of the inner active damping loop stability is that the magnitude at the cross-over frequency f_h is tuned to be below 0 dB. With this stability criterion, the parameters of the damping factor ξ and natural frequency ω_n can be confirmed.

The cross-over frequency f_h can be obtained by solving the following equation:

$$1.5\omega_h T_s + \arctan\frac{\xi\omega_n\omega_h}{\omega_n^2 - \omega_h^2} = \pi \tag{13}$$

Equation (13) represents that the phase characteristic crosses over −180° at the frequency f_h. No matter what the coefficients ξ and ω_n are, the cross-over frequency should be larger than the resonance frequency. According to the Nyquist stability criterion, the inner loop can be stable without negative crossing at the resonance frequency. The influence of the two coefficients variation on the inner active damping loop stability is illustrated in Fig. 7(b) and 7(c). In Fig. 7(b), k=1 and $\omega_n = \omega_r$. When the damping factor ξ increases, the phase characteristic becomes smooth. The magnitudes of the low-frequency and high-frequency regions increase. Especially, the cross-over frequency f_h increases, which improves the inner loop stability margin. In Fig. 7(c), k=1 and $\xi = 1$. When the natural frequency ω_n increases, the magnitudes of the low-frequency region decrease and the magnitudes of the high-frequency region increase. Most importantly, the cross-over frequency increases. Therefore, a proper damping factor ξ and natural frequency ω_n can be obtained by plotting Bode diagrams with this stability criterion.

After obtaining the damping factor ξ and natural frequency ω_n, the stable range for k should be discussed. The variation of k only affects the gain of the inner active damping loop. The pole maps can help further determine the range of the coefficient k which improves the inner active damping loop stability.

In Fig. 8, p_1 and p_2 are the complex-conjugate resonance poles whose damping ratios are quite small. As can be seen, when $k = 0$, the poles are located in a unit circle. The bigger the coefficient k is, the higher the frequency of the resonance pole location becomes. Furthermore, the damping ratios of p_1 and p_2 vary. A rule of thumb is to select a value for the coefficient k which makes the damping ratio biggest. Then the potential resonance danger can be prevented. In summary, with the two criteria, proper SORI parameters can be obtained.

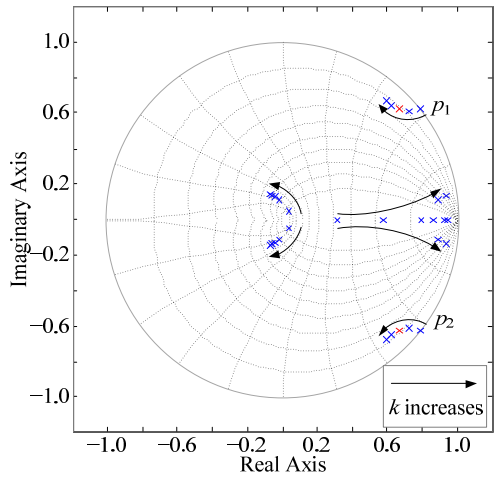

Fig. 8. Active damping loop pole map with a k variation.

B. Design Example

After the above design procedure, under the premise of ensuring the stability of the active damping loop, the design of the PR controller adopts the optimized design (OP) method [27]. In the discrete domain, the parameters of the OP method are tuned to have the following values:

TABLE II. PARAMETERS OF THE PR CONTROLLER AND SORI FILTER

Test Case	Case A f_r/f_s=0.225	Case B f_r/f_s=0.167	Case C f_r/f_s=0.11
PR Controller (k_p)	5.0	3.9	2.9
PR Controller (k_r)	150	150	150
SORI Filter(k)	2	4	6
SORI Filter(ξ)	2	2	2
SORI Filter(ω_n)	$2\omega_r$	$2\omega_r$	$2\omega_r$

$$k_p = \frac{\omega_c (L_1 + L_2)}{K_{pwm}}, k_r = \frac{\omega_c}{10} \tag{14}$$

where ω_c is the crossover angular frequency that can be chosen as $\omega_c \approx 0.3\omega_r$ [28]. In addition, the overshoot to the step input should be lower than the expected 10%.

The influence of the SORI filter proportional coefficient k and current regulator parameters on the control loop bandwidth and stability margin is determined. This helps to guide the selection of the parameters. Since the crossover frequency f_c is lower than f_r, the effect of the filter capacitor C_f can be ignored while calculating the magnitude of the loop gain at frequencies up to f_c [32], [33]. According to equation (3), the magnitude of the current loop gain can be simplified as:

$$|T_c(s)| \approx \left| \frac{G_i(s) K_{PWM}}{s(L_1 + L_2)} \right| \tag{15}$$

Meanwhile, the magnitude of the PR regulator can be simplified as $|G_i(s)| \approx k_p$. Letting $|T_c(j2\pi f_c)|=1$ yields:

$$k_p \approx \frac{2\pi (L_1 + L_2)}{K_{PWM}} f_c \tag{16}$$

This simplified proportional coefficient k_p is the same as the OP method shown in equation (14). The crossover frequency f_c is almost proportional to the coefficient k_p. Hence, a larger k_p means a faster dynamic response and a larger loop gain at low frequencies.

The possible regions of k_p and k_r are obtained under the specifications of the stability margins. The open-loop transfer function of this current loop in the continuous domain is given as:

$$\begin{aligned} T_{col}(s) &= \frac{G_i(s) G_d(s) K_{PWM} G_{LCL}(s)}{1 + G_d(s) K_{PWM} G_{LCL}(s) H(s)} \\ &= \frac{G_i(s)(s^2 + \xi\omega_n s + \omega_n^2) e^{-1.5sT_s}}{(L_1 L_2 C_f s^3 + L_T s)(s^2 + \xi\omega_n s + \omega_n^2) - k\xi\omega_n s e^{-1.5sT_s}} \end{aligned} \tag{17}$$

where L_T=L_1+L_2.

Since the crossover frequency f_c is high enough when compared with f_o and $\omega_i/2\pi$, the regulator $G_i(s)$ can be simplified as $G_i(s) \approx k_p + 2k_r\omega_i/s$ to calculate the phase margin (PM) at f_c. Substituting $s = j2\pi f_c$ into (17), the expression of the PM can be derived as:

$$\begin{aligned} PM = \frac{\pi}{2} - 3\pi f_c T_s - \arctan\frac{k_r \omega_i}{\pi f_c k_p} \\ - \arctan\frac{\xi\omega_n\omega_c}{\omega_c^2 - \omega_n^2} - \arctan\frac{D}{E} \end{aligned} \tag{18}$$

where:

$$\begin{aligned} D &= \omega_c L_T \xi\omega_n + k\xi\omega_n \sin(3\pi f_c T_s) - \omega_c^3 L_1 L_2 C_f \xi\omega_n, \\ E &= \omega_c^4 L_1 L_2 C_f - \omega_c^2 (L_1 L_2 C_f \omega_n^2 + L_T) \\ &\quad + L_T \omega_n^2 - k\xi\omega_n \cos(3\pi f_c T_s) \end{aligned}$$

According to (16), the boundary of the current regulator resonant coefficient k_r with respect to f_c under the PM constraint can be derived as (19), as shown at the bottom of the page.

According to (19), taking case C as an example, the possible regions of k_r and f_c for different filter coefficients k are drawn in Fig. 9, using the parameters listed in Table II.

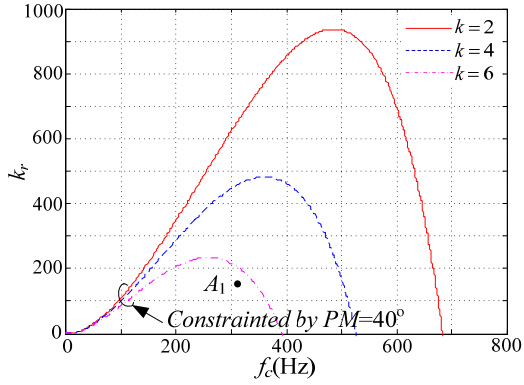

Fig. 9. PM=40°, region of k_r and f_c constrained by a PM with a different k for case C.

As can be seen, the region becomes larger when the SORI filter proportional coefficient k is reduced. However, according to the tuning method of the SORI filter in Section IV-A, the coefficient k should be selected at a bigger damping ratio pole in a unit circle. For case C, when ξ=2 and ω_n=2ω_r, the coefficient k can be obtained by a pole map, i.e., k=6. Thus, point A_1 is chosen as the optimized controller parameter for case C. For cases A, B and C, the PR controller and SORI filter parameters are listed in Table II.

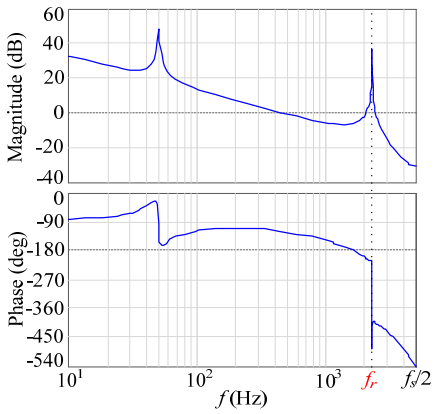

(a)

method for three different *LCL* resonance frequencies. The tuning parameters are listed in Table II. In Fig. 10(a), $f_r > f_s/6$. Since the resonance peak is highly cut down, the grid current loop can obtain a higher crossover frequency with the proposed AD method under the same phase margin. Compared with Fig. 3, the stabilities of cases B and C are greatly improved. For $f_r \le f_s/6$, as shown in Fig. 10(b) and 10(c), the phase characteristics cross -180° outside the region whose amplitudes are positive. Moreover, the resonance peak is basically lower than 0 dB which helps improve the dynamic performance.

V. Experimental Results

For verification, a 1.5kW test setup was built and tested in the laboratory. The grid voltage v_g, which is used in the PLL, is sensed by two voltage transducers. The grid current i_2 is sensed by two current transducers. All of the signals are sampled by a 14-b analog-to-digital converter (MAXIM-1324ECM). The current controller and the proposed active damping are implemented with a TI TMS320F28335 DSP. The key parameters of the test setup are listed in Tables I and II.

$$k_r = 2\pi^2 f_c^2 L_T \cdot \frac{E(\omega_c^2-\omega_n^2) - D\xi\omega_n\omega_c - [D(\omega_c^2-\omega_n^2) + E\xi\omega_n\omega_c]\cdot\tan(PM + 3\pi f_c T_s)}{E(\omega_c^2-\omega_n^2)\omega_i \tan(PM + 3\pi f_c T_s) + D\omega_i(\omega_c^2-\omega_n^2) + E\omega_i\xi\omega_n\omega_c} \quad (19)$$

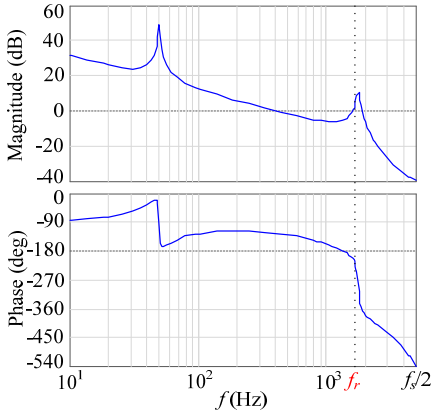

(b)

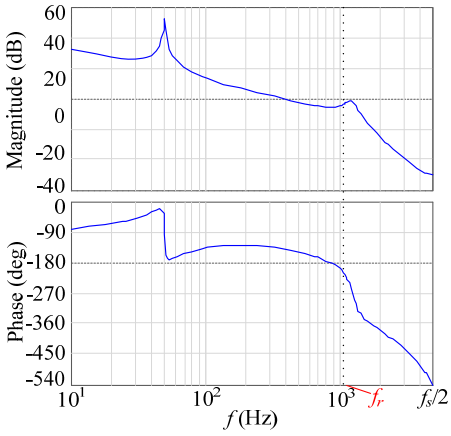

(c)

Fig. 10. Grid current open-loop Bode diagrams of the proposed AD method for three different cases: (a) Case A: C_f=12μF. (b) Case B: C_f=22μF. (c) Case C: C_f=50μF.

According to the previous design guidelines, Fig. 10 shows grid current open-loop Bode diagrams with the proposed AD

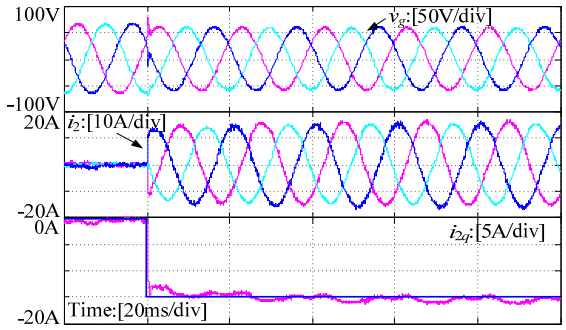

(a)

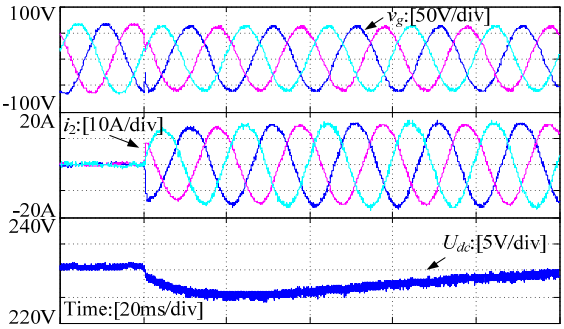

(b)

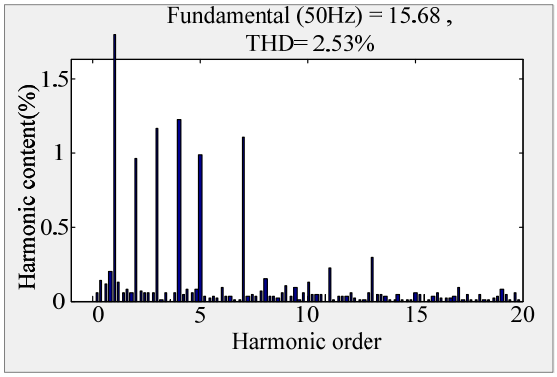

(c)

Fig. 11. Experimental results for case A: (a) Transient results when the reactive current steps between 0 and -15A. (b) Grid-side current in view of a dc-load step from no-load to full-load. (c) FFT analysis of the current under the full-load situation.

Fig. 11 shows experimental results for case A when the resonance frequency is $0.225f_s$. Among the three cases, the bandwidth of the current loop for case A is the highest. The system can obtain a good dynamic performance when given a current mutation instruction. The overshoot to the step input is lower than the expected 10%. Moreover, the rising time is also acceptable. The controller parameters meet the technical indexes of the dynamic performance. Under the full-load condition, the resonance peak can be well damped and the system achieves good steady state performance. The experimental results confirm the effectiveness of the proposed AD method and the correctness of the proposed tuning procedure. Fig. 11(c) shows the harmonic spectrum of the injected grid current.

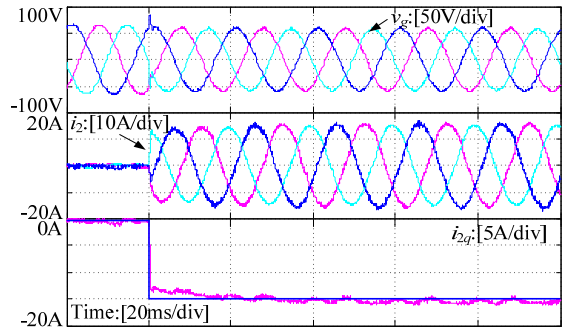

(a)

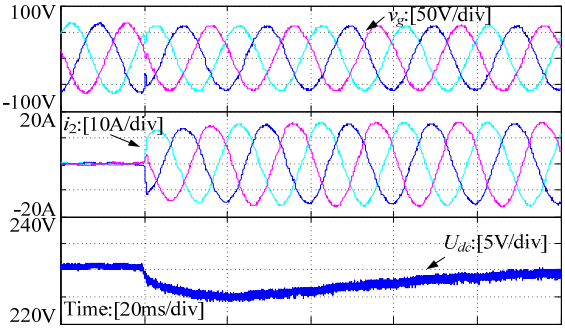

(b)

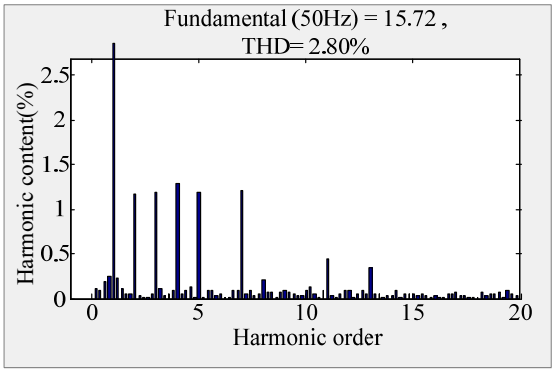

(c)

Fig. 12. Experimental results for case B: (a) Transient results when the reactive current steps between 0 and -15A. (b) Grid-side current in view of a dc-load step from no-load to full-load. (c) FFT analysis of the current under the full-load situation.

As shown in Fig. 12, with the proposed AD method, the experimental results for case B can also achieve good transient and steady-state performances. The tracking experimental waveform of the q axis current is shown in Fig. 12(a). The reactive current reference change from 0 to -15A and the actual reactive current tracks its reference well. In Fig. 12(b), with the load current feedforward, the dc voltage rapidly returns to the reference and only has a small voltage drop. Fig. 12(c) shows the harmonic content of the injected grid current. The total harmonic distortion (THD) is 2.8%, which satisfies the relevant requirements for grid-tied converters.

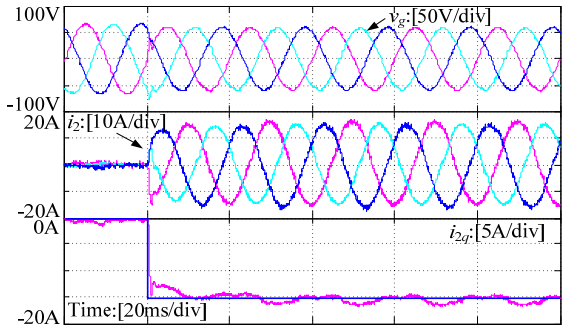

(a)

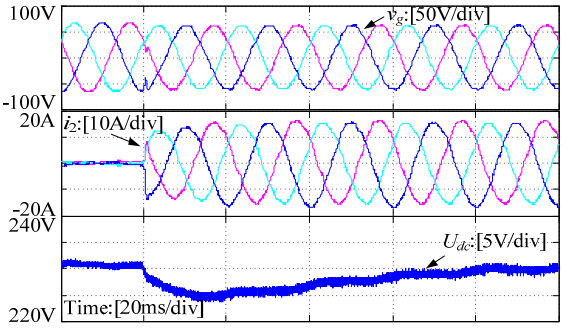

(b)

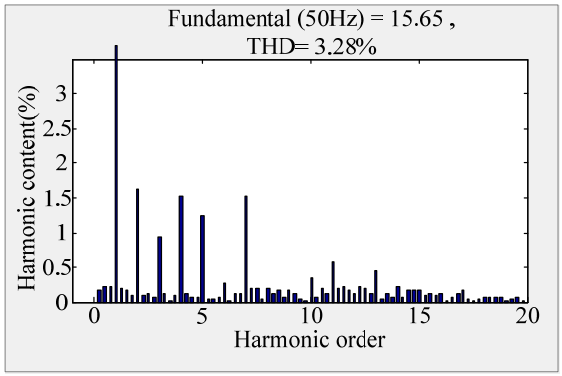

(c)

Fig. 13. Experimental results for case C: (a) Transient results when the reactive current steps between 0 and -15A. (b) Grid-side current in view of a dc-load step from no-load to full-load. (c) FFT analysis of the current under the full-load situation.

Compared with Fig. 11 and Fig. 12, Fig. 13 shows more oscillatory transient grid current waveforms. Even so, with the proposed tuning method in Section IV, the system can achieve the expected steady-state performance. Fig. 13(c) shows the harmonic spectrum of the injected grid current.

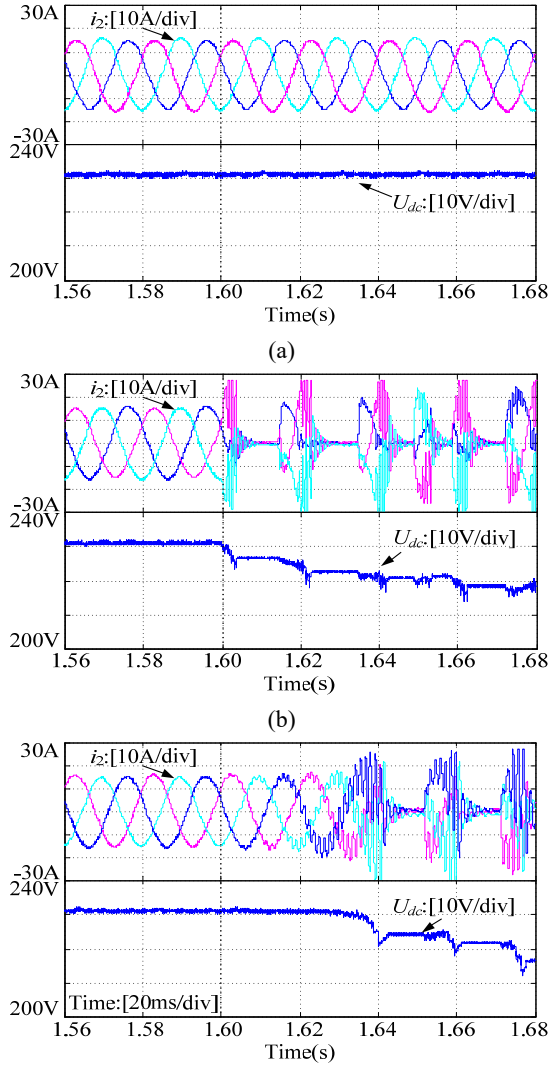

(a)

(b)

(c)

Fig. 14. The comparative experimental results for with and without the proposed AD method for three different cases: (a)Case A, f_r/f_s=0.225. (b) Case B, f_r/f_s=0.167. (c) Case C, f_r/f_s =0.11.

In order to further validate the performance of the proposed AD method, an experimental comparison of with and without the proposed method is shown in Fig. 14. Under the three different circumstances, the experimental results are different. For case A, the resonance frequency f_r is higher than $f_s/6$. According to the previous stability analysis, the active damping is not required, i.e., a system with a high resonance frequency region can be stable without any AD method. As shown in Fig. 14(a), the control scheme changes from with the proposed AD method to without the proposed AD method at 1.6s. This experimental waveform validates the theoretical analysis. When the resonance frequency is a critical frequency, as illustrated in Fig. 14(b), the system cannot be stable without a damper. The control method is switched at 1.6s. Then a disastrous oscillation is triggered. The dc link voltage collapses. This confirms that the AD method should be introduced to suppress the oscillation. A low resonance frequency can also cause instability of the system. In Fig. 14(c), the resonance frequency is lower than $f_s/6$. The grid currents start to oscillate at 1.6s and they diverge after about two fundamental periods. For the low resonance frequency region, the AD method is mandatory to maintain system stability and current quality.

In summary, under the premise of using the same number of sensors, the system can also obtain a good control effect with the proposed AD method. Therefore, experimental results validate concepts presented in this paper.

VI. Conclusion

A novel AD scheme based on injected grid current feedback has been proposed for *LCL*-type grid-connected converters. The derivation of the proposed AD scheme is based on the MRAC. This paper presents a detailed derivation processes. By an equivalent transformation, the proposed AD scheme is essentially used to introduce a SORI filter into the grid current feedback loop.

The proposed AD scheme does not need additional sensors which reduces cost. It can suppress the resonance peak with only grid-current feedback control. In addition, it can achieve expected steady-state and transient performances. A straightforward design procedure has been presented while considering the inherent one-step delay in the digital control system. Experimental results show the anticipated steady state and transient performances. Therefore, the proposed AD scheme is validated.

References

[1] M. Lindgren and J. Svensson, “Control of a voltage-source converter connected to the grid through an *LCL*-filter-application to active filtering,” in *Proc. Rec. 29th Annu. IEEE Power Electron. Spec. Conf. (PESC’98)*, vol. 1, 1998, pp. 229–235.

APPENDIX

$$20\lg\left|T_{ol\_ad}(s)\right|_{s=j\omega}\Big| = 20\lg\left|e^{-j1.5\omega T_s}K_{PWM}\frac{1}{L_1L_2C_f\,j\omega\left(\omega_r^2-\omega^2\right)}\frac{-k\xi\omega_n\,j\omega}{\omega_n^2-\omega^2+j\xi\omega_n\omega}\right| = 20\lg\left(\frac{K_{PWM}}{L_1L_2C_f\left|\omega_r^2-\omega^2\right|}\frac{k\xi\omega_n}{\sqrt{\left(\omega_n^2-\omega^2\right)^2+\left(\xi\omega_n\omega\right)^2}}\right) \tag{A.1}$$

$$\angle T_{ol\_ad}(s)\Big|_{s=j\omega} = \angle e^{-j1.5\omega T_s}K_{PWM}\frac{1}{L_1L_2C_f\left(\omega_r^2-\omega^2\right)}\frac{-k\xi\omega_n}{\omega_n^2-\omega^2+j\xi\omega_n\omega} = \begin{cases}\pi-1.5\omega T_s-\arctan\dfrac{\xi\omega_n\omega}{\omega_n^2-\omega^2}, \omega<\omega_r\\ -1.5\omega T_s-\arctan\dfrac{\xi\omega_n\omega}{\omega_n^2-\omega^2}, \omega>\omega_r\end{cases} \tag{A.2}$$

[2] M. Liserre, F. Blaabjerg, and S. Hansen, "Design and control of an *LCL* filter-based three-phase active rectifier," *IEEE Trans. Ind. Appl.*, vol. 41, no. 5, pp. 1281–1291, Sep./Oct. 2005.

[3] R. Pena-Alzolaet al., "Analysis of the passive damping losses in *LCL*-filter based grid converters," *IEEE Trans. Power Electron.*, vol. 28, no. 6, pp. 2642–2646, Jun. 2013.

[4] I. J. Gabe, V. F. Montagner, and H. Pinheiro, "Design and implementation of a robust current controller for VSI connected to the grid through an *LCL* filter," *IEEE Trans. Power Electron.*, vol. 24, no. 6, pp. 1444–1452, Jun. 2009.

[5] D. Pan, X. Ruan, C. Bao, W. Li, and X. Wang, "Optimized Controller Design for *LCL*-Type Grid-Connected Inverter to Achieve High Robustness against Grid-Impedance Variation," *IEEE Trans. Ind. Electron.*, vol. 62, no. 3, pp. 1537-1547, Mar. 2015.

[6] J. Dannehl, F. W. Fuchs, and P. B. Thøgersen, "PI state space current control of grid-connected PWM converters with *LCL* filters," *IEEE Trans. Power Electron.*, vol. 25, no. 9, pp. 2320–2330, Sep. 2010.

[7] C. Bao, X. Ruan, X. Wang, W. Li, D. Pan, and K. Weng, "Step-by-step controller design for *LCL*-type grid-connected inverter with capacitor-current-feedback active-damping," *IEEE Trans. Power Electron.*, vol. 29, no. 3, pp. 1239−1253, Mar. 2014.

[8] A. Ghoshal and V. John, "Active damping of LCL filter at low switching to resonance frequency ratio," *IET Power Electron*., vol. 8, pp. 574–582, 2015.

[9] G. Shen, D. Xu, L. Cao, and X. Zhu, "An improved control strategy for grid-connected voltage source inverters with a *LCL* filter," *IEEE Trans. Power Electron.*, vol. 43, no. 5, pp. 1899–1906, Jul. 2008.

[10] Y. Tang, P. C. Loh, P. Wang, F. H. Choo, and F. Gao, "Exploring inherent damping characteristic of *LCL*-filters for three-phase grid-connected voltage source inverters," *IEEE Trans. Power Electron*., vol. 27, no. 3, pp. 1433–1443, Mar. 2012.

[11] J. Dannehl, C. Wessels, and F. W. Fuchs, "Limitations of voltage-oriented PI current control of grid-connected PWM rectifiers with *LCL* filters," *IEEE Trans. Ind. Electron.*, vol. 56, no. 2, pp. 380–388, Feb. 2009.

[12] J. Yin, S. Duan, and B. Liu, "Stability analysis of grid-connected inverter with *LCL* filter adopting a digital single-loop controller with inherent damping characteristic," *IEEE Trans. Ind. Informat*., vol. 9, no. 2, pp. 1104–1112, May 2013.

[13] J. R. Massing, M. Stefanello, H. A. Grundling, and H. Pinheiro, "Adaptive current control for grid-connected converters with *LCL* filter," *IEEE Trans. Ind. Electron.*, vol. 59, no. 12, pp. 4681–4693, Dec. 2012.

[14] P. Rodriguez, R. Teodorescu, I. Candela, A. V. Timbus, M. Liserre, and F. Blaabjerg, "New positive-sequence voltage detector for grid synchronization of power converters under faulty grid conditions," in Proc. IEEE Power Electron. Spec. Conf., Jun. 2006, pp. 1–7.

[15] M. Ciobotaru, R. Teodorescu, and F. Blaabjerg, "A new single-phase PLL structure based on second order generalized integrator," in Proc. IEEE Power Electron. Spec. Conf., Jun. 2006, pp. 1–6.

[16] S. Golestan, M. Monfared, and F. D. Freijedo, "Design-oriented study of advanced synchronous reference frame phase-locked loops," *IEEE Trans. Power Electron.*, vol. 28, no. 2, pp. 765–778, Feb. 2013.

[17] P. Rodriguez, A. Luna, M. Ciobotaru, R. Teodorescu, and F. Blaabjerg, "Advanced grid synchronization system for power converters under unbalanced and distorted operating conditions," in Proc. IEEE 32nd Ind. Electron. Soc., Paris, France, Nov. 6–10, 2006, pp. 5173–5178.

[18] P. Rodriguez, A. Luna, R. S. Munoz-Aguilar, I. Etxeberria-Otadui, R. Teodorescu, and F. Blaabjerg, "A stationary reference frame grid synchronization system for three-phase grid-connected power converters under adverse grid conditions," IEEE Trans. Power Electron., vol. 27, no. 1, pp. 99–112, Jan. 2012.

[19] P. Rodriguez, A. Luna, I. Candela, R. Mujal, R. Teodorescu, and F. Blaabjerg, "Multiresonant frequency-locked loop for grid synchronization of power converters under distorted grid conditions," IEEE Trans. Ind. Electron., vol. 58, no. 1, pp. 127–138, Jan. 2011.

[20] X. Yuan, W. Merk, H. Stemmler, and J. Allmeling, "Stationary-frame generalized integrators for current control of active power filters with zero steady-state error for current harmonics of concern under unbalanced and distorted operating conditions," IEEE Trans. Ind. Appl., vol. 38, no. 2, pp. 523–532, Mar./Apr. 2002.

[21] G. Fedele, C. Picardi, and D. Sgro, "A power electrical signal tracking strategy based on the modulating functions method," IEEE Trans. Ind. Electron., vol. 56, no. 10, pp. 4079–4087, Oct. 2009.

[22] M. Ciobotaru, V. G. Agelidis, R. Teodorescu, and F. Blaabjerg, "Accurate and less-disturbing active antiislanding method based on PLL for gridconnected converters," IEEE Trans. Power Electron., vol. 25, no. 6, pp. 1576–1584, Jun. 2010.

[23] F. D. Freijedo, J. Doval-Gandoy, O. Lopez, and E. Acha, "Tuning of phase locked loops for power converters under distorted utility conditions," *IEEE Trans. Ind. Appl.*, vol. 45, no. 6, pp. 2039–2047, Dec. 2009.

[24] M. Liserre, R. Teodorescu, and F. Blaabjerg, "Stability of

photovoltaic and wind turbine grid-connected inverters for a large set of grid impedance values," IEEE Trans. Power Electron., vol. 21, no. 1, pp. 263–272, Jan. 2006.
[25] J. L. Agorreta, M. Borrega, J. Lopez, and L. Marroyo, "Modeling and control of N-paralleled grid-connected inverters with *LCL* filter coupled due to grid impedance in PV plants," *IEEE Trans. Power Electron.*, vol. 26, no. 3, pp. 770–785, Mar. 2011.
[26] S. G. Parker, B. P. McGrath, and D. G. Holmes, "Regions of active damping control for *LCL* filters," *IEEE Trans. Ind. Appl.*, vol. 50, no. 1, pp. 424–432, Jan./Feb. 2014.
[27] D. G. Holmes, T. A. Lipo, B. P. McGrath, and W. Y. Kong, "Optimized design of stationary frame three phase AC Current regulators," *IEEE Trans. Power Electron.*, vol. 24, no. 11, pp. 2417–2426, Nov. 2009.
[28] Y. Tang, P. C. Loh, P. Wang, F. H. Choo, F. Gao, and F. Blaabjerg, "Generalized design of high performance shunt active power filter with output *LCL* filter," *IEEE Trans. Ind. Electron.*, vol. 59, no. 3, pp. 1443–1452, Mar. 2012.
[29] R. Pena Alzola, M. Liserre, F. Blaabjerg, R. Sebastian, J. Dannehl, and F. W. Fuchs, "Systematic design of the lead-lag network method for active damping in lcl-filter based three phase converters," IEEE Trans. Ind. Inf., vol. 10, no. 1, pp. 43–52, Feb. 2014.
[30] Z. Xin, X. Wang, P. C. Loh, and F. Blaabjerg, "SOGI-Based Capacitor Voltage Feedback Active Damping in LCL-Filtered Grid Converters," in 6th International Symposium on Power Electronics for Distributed Generation Systems, Aachen, Germany, 2015.
[31] X. Wang, F. Blaabjerg, and P. C. Loh, "Virtual RC damping of LCL filtered voltage source converters with extended selective harmonic compensation," IEEE Trans. Power Electron., vol. 62, no. 3, pp. 1537–1547, Mar. 2015.
[32] D. Yang, X. Ruan, and H. Wu, "A real-time computation method with dual sampling modes to improve the current control performance of the LCL-type grid-connected inverter," IEEE Trans. Ind. Electron., vol. 62, no. 7, pp. 4563–4572, Jul. 2015.
[33] C. Chen, J. Xiong, Z. Wan, J. Lei and K. Zhang, "Time Delay Compensation Method Based on Area Equivalence For Active Damping of an LCL-Type Converter," IEEE Trans. Power Electron., vol. 32, no. 1, pp. 762–772, Jan. 2017.

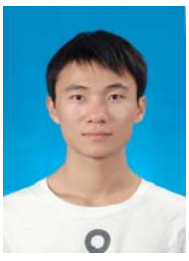

Chen Chen received his B.S. degree from Jiangsu University, Zhenjiang, China, in 2012. He is presently working towards his Ph.D. degree in the School of Electrical and Electronics Engineering, Huazhong University of Science and Technology (HUST), Wuhan, China. His current research interests include digital control techniques, power converters design and control, high power factor rectifiers, grid integration of distributed generation and renewable resources, and modular multilevel converters.

Jian Xiong received his B.S. degree from the East China Shipbuilding Institute, Zhenjiang, China, in 1993; and his M.S. and Ph.D. degrees from the Huazhong University of Science and Technology (HUST), Wuhan, China, in 1996 and 1999, respectively. He joined HUST as a Lecturer in 1999, and became an Associate Professor in 2003. His current research interests include uninterruptible power systems, ac drives, switch-mode rectifiers, STATCOMs, and their related control techniques.

Kai Zhang received his B.S., M.S. and Ph.D. degrees from the Huazhong University of Science and Technology (HUST), Wuhan, China, in 1993, 1996 and 2001, respectively. He joined HUST as an Assistant Lecturer in 1996, and was promoted to Full Professor in 2006. He was a Visiting Scholar at the University of New Brunswick, Fredericton, NB, Canada, from 2004 to 2005. He is the author of more than 60 technical papers. His current research interests include uninterruptible power systems, railway traction drives, modular multilevel converters, and electromagnetic compatibility techniques for power electronic systems.